

Multiprincipal Component P2-Na_{0.6}(Ti_{0.2}Mn_{0.2}Co_{0.2}Ni_{0.2}Ru_{0.2})O₂ as a High-Rate Cathode for Sodium-Ion Batteries

Lufeng Yang,[#] Chi Chen,[#] Shan Xiong, Chen Zheng, Pan Liu, Yifan Ma, Wenqian Xu, Yuanzhi Tang, Shyue Ping Ong,^{*} and Hailong Chen^{*}

Cite This: <https://dx.doi.org/10.1021/jacsau.0c00002>

Read Online

ACCESS |

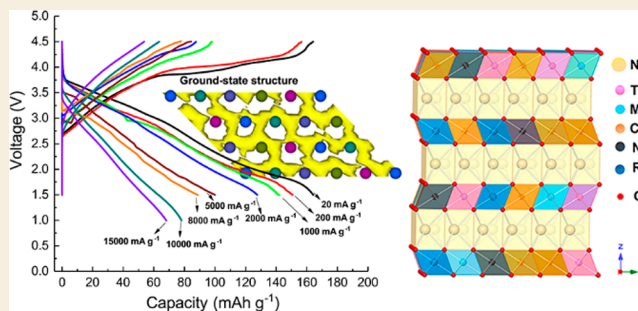
Metrics & More

Article Recommendations

Supporting Information

ABSTRACT: Mixing transition metal cations in nearly equiatomic proportions in layered oxide cathode materials is a new strategy for improving the performances of Na-ion batteries. The mixing of cations not only offers entropic stabilization of the crystal structure but also benefits the diffusion of Na ions with tuned diffusion activation energy barriers. In light of this strategy, a high-rate Na_{0.6}(Ti_{0.2}Mn_{0.2}Co_{0.2}Ni_{0.2}Ru_{0.2})O₂ cathode was designed, synthesized, and investigated, combining graph-based deep learning calculations and complementary experimental characterizations. This new cathode material delivers high discharge capacities of 164 mA g⁻¹ at 0.1 C and 68 mAh g⁻¹ at a very high rate of 86 C, demonstrating an outstanding high rate capability. *Ex situ* and *operando* synchrotron X-ray diffraction were used to reveal the detailed structural evolution of the cathode upon cycling. Using the climbing-image nudged elastic-band calculation and *Ab initio* molecular dynamics simulations, we show that the optimal transition metal composition enables a percolating network of low barrier pathways for fast, macroscopic Na diffusion, resulting in the observed high rate performance.

KEYWORDS: Na-ion battery, cathode, high entropy, high rate, transition metal oxide, AIMD, ionic diffusivity



1. INTRODUCTION

Sodium (Na)-ion batteries (NIBs) are attracting a great deal of interest for large-scale energy storage applications owing to the advantages in manufacturing cost over Li-ion batteries (LIBs). Layered sodium transition metal (TM) oxides with the general formula Na_xMO₂ (M = Co, Ni, Mn, Fe, V, or Cr) have been extensively studied as cathodes for NIBs for their low cost and high theoretical capacities.¹ In contrast to their counterpart LiMO₂, which most often crystallizes only in O3-type layered structures, Na_xMO₂ presents more stable or metastable crystal structures with a different coordination of Na (prismatic or octahedral) and a different stacking sequence, with P2 and O3 being the two most extensively explored.^{1,2} Theoretical evaluation indicates that P2 structures have Na diffusion barriers lower than those of O3 structures.^{3,4} However, the rate performance of P2-structured cathodes is often hindered by Na ordering or phase transformation upon Na⁺ (de)-intercalation.^{5,6} In P2-type Na_xMO₂, Na ions occupy two types of prismatic sites: the Na(f) site, sharing faces with two adjacent MO₆ octahedra, and the Na(e) site, sharing only edges with MO₆ octahedra. The Na mobility between the two sites can be affected by the repulsive Na⁺-Na⁺ interaction and charge ordering in the transition metal layer. Therefore, the distinctive Na⁺/vacancy superstructures (Na ordering) at various Na concentrations could have different impacts on

the diffusivity.^{5,7-9} The transition between the superstructures upon Na removal results in voltage plateaus in the electrochemical curves, which sometimes lower the Na⁺ diffusion coefficient by up to 2 orders of magnitude⁹ and thus degrade the rate performance.^{6,10,11} In addition to Na ordering, stacking changes during cycling, such as the commonly seen P2-O2 transition, can also result in a stepwise voltage profile and cause inhomogeneous electrochemical reaction in the electrode.¹² Such stacking transformations may not be fully reversible and can produce dislocations and microcracks,^{13,14} which harm the rate performance and cycling life as well. The Na⁺/vacancy ordering is significantly impacted by charge ordering/distribution in the TM layer.^{5,6,15} Therefore, from a material design point of view, trying to tune the elemental composition in the charge distribution in the transition metal layer to reduce the phase transition and Na-ordering in cycling should be an effective strategy benefiting both the rate performance and cycling life. Some previous reports have

Received: August 25, 2020

demonstrated promise along this direction. Our previous work on phase-transition-free cathodes^{13,16} showed very high capacity and good retention. Liu et al.¹⁷ reported a P2-type $\text{Na}_{2/3}(\text{Mn}_{1/2}\text{Fe}_{1/4}\text{Co}_{1/4})\text{O}_2$ cathode with superior rate performance by creating large regions of solid solution in the materials upon sodiation/desodiation. Wang et al.¹¹ also showed that the disordered arrangement of Na vacancies within Na layers in $\text{Na}_{2/3}\text{Ni}_{1/3}\text{Mn}_{1/3}\text{Ti}_{1/3}\text{O}_2$ induced by Ti^{4+} doping in TM layers leads to fast Na mobility and a low Na diffusion barrier. Lin et al. reported a number of multiple-cation cathodes and their surface interactions with electrolytes.^{18–21} A computational study by Zheng et al.²² showed that mixing TMs in layered compounds can reduce the energetic differences between Na orderings and suppress Na-vacancy ordering.

On the other hand, synthesis of a P2-cathode with multiple metal cations is often challenging as the phase diagrams are quite complicated even for the case where only one metal is used.²³ The emerging multiprincipal component alloys²⁴ and ceramics,²⁵ sometimes noted as high entropy alloys and ceramics, provide a new possibility of stabilizing the P2-structure. With the higher configuration entropy offered by multiprincipal components, many compounds can be stabilized in high-temperature synthesis due to reduced formation enthalpy. A few high entropy materials have been tested as the anode²⁶ or cathode²⁷ in batteries and showed good performance. Here, guided by the strategy of reducing Na-ordering and phase transition and taking advantage of cation mixing in TM layers, we designed a novel multiprincipal component (MPC) P2-structured cathode, $\text{Na}_{0.6}(\text{Ti}_{0.2}\text{Mn}_{0.2}\text{Co}_{0.2}\text{Ni}_{0.2}\text{Ru}_{0.2})\text{O}_2$ (P2-TMCNR), and successfully synthesized it in the lab with the help of *in situ* X-ray diffraction for synthesis. This material exhibits an outstanding rate performance, delivering a high capacity of 164 mAh g^{-1} at 0.1 C and a capacity of 68 mAh g^{-1} at a very high rate of 86 C, exceeding most existing Na cathodes. Both experimental characterizations and computational evaluations endorsed that the design strategy was successful in this material and could be more widely impactful for the design of layered oxide cathodes and the development of high power, high energy Na-ion batteries.

2. EXPERIMENTAL AND COMPUTATIONAL METHODS

2.1. Experimental Section

Materials Preparation. The P2-TMCNR compound was synthesized via solid-state reaction from starting materials of sodium carbonate (Na_2CO_3 , Alfa Aesar, 99.7%), titanium oxide (TiO_2 , Aldrich, 99.7%), ruthenium oxides (RuO_2 , Alfa Aesar, 99.9%), cobalt hydroxide ($\text{Co}(\text{OH})_2$, Alfa Aesar, 99.9%), nickel hydroxide ($\text{Ni}(\text{OH})_2$, Alfa Aesar, Ni 61%), and manganese oxide (MnO_2 , Alfa Aesar, 99.7%) with stoichiometric ratios. The sodium sources were used in 5% excess to compensate for the loss in high-temperature calcination. The starting materials were mixed and ground by using a planetary high-energy ball mill (Retsch PM200) at 300 rpm for 2 h. The mixture was then pressed into pellets and calcined in air at 850 °C for 12 h with a ramping rate of 5 °C per minute. After calcination, the pellets were quenched to room temperature on a copper plate. The quenched pellets were then transferred to an Ar-filled glovebox immediately to minimize contact with air and moisture.

Electrochemical Testing. P2-TMCNR active material (85 wt %) and carbon black (15 wt %, Super P, Timcal) were first mixed in a Retsch PM200 planetary ball-mill at 300 rpm for 2 h. Positive electrode slurry was then prepared by mixing the ball-milled active material (80 wt %) with carbon black (10 wt %, Super C65,

TIMCAL) and polyvinylidene difluoride (PVDF, 10 wt %, 6020 Solef, Arkema Group) in *N*-methyl-2-pyrrolidone (NMP). The slurry was cast onto an aluminum foil and dried at 100 °C in a vacuum oven overnight. The dried film was roll-pressed and cut into round disks of 15 mm diameter. The mass loading of active material is 1–2 mg/cm^2 . Sodium metal foil was used as the negative electrodes. One M NaPF_6 dissolved in propylene carbonate (PC) was used as the electrolyte, and a piece of glass fiber filter GF/D (Whatman) was used as the separator. CR2016-type coin cells were then assembled in an Ar-filled glovebox and tested with Land battery cyclers and an Arbin battery cycler (BT2043).

Materials Characterization. To determine the best synthesis condition for the desired P2 phase, *in situ* X-ray diffraction (XRD) for synthesis was performed using an HTK1200N temperature chamber installed on a Bruker D8 Advance diffractometer. At each designed temperature, the temperature was held for 1 h for the XRD pattern collection. *Operando* XRD of the samples was performed on the Bruker D8 Advance diffractometer equipped with a molybdenum source ($\lambda = 0.709 \text{ \AA}$). The *in situ* cell was charged/discharged within a voltage domain of 1.5–4.5 V at a rate of C/30. Each scan covered a 2θ range of 6.5–23° in a time duration of 5000 s. The electrochemical cell used for the *operando* XRD measurement is similar to those used in our previous publication.²⁸ Selected powder samples were also tested using the synchrotron radiation source ($\lambda = 0.4539 \text{ \AA}$) at beamline 17-BM at the Advanced Photon Source (APS) at Argonne National Laboratory (ANL). Some additional synchrotron experiments were also performed using 28-ID-2 beamline of the National Synchrotron Light Source II (NSLS-II) at Brookhaven National Laboratory and the 7-2 beamline of Stanford Synchrotron Radiation Lightsource (SSRL). Morphological investigation and energy-dispersive X-ray spectroscopy (EDS) mapping analysis of the samples was conducted using a field emission scanning electron microscopy (FE-SEM, Zeiss, Ultra60).

2.2. Computational Section

Finding the Structural Configurations with Lowest Energies. Given a large number of TM cations, the combinatorial space of TM orderings coupled with Na/vacancy orderings is far too large to be evaluated directly via DFT calculations. To obtain low-energy structures, Monte Carlo (MC) simulated annealing was performed using a surrogate energy model. Previously, the current authors developed a MatErials Graph Network (MEGNet) deep learning model²⁹ that can predict the formation energies of Materials Project crystals within a state-of-the-art mean absolute error of 28 meV/atom. The MEGNet model featurizes the materials into graphs with the atoms as nodes, bonds as edges, and state attributes as global information. Subsequently, the graphs are passed to graph convolutions and finally to the output properties. The formation energy MEGNet model previously developed by the coauthors, which was trained using 69 239 structure-energy pairs from the June 2018 version of the Materials Project³⁰ database, was used as is in this work without further refitting. The model prediction uses computational structures rescaled to the experimental lattice parameters, with each prediction taking ~ 0.03 s. We started from the well-known Na vacancy configuration pattern for P2- $\text{Na}_{0.6}\text{CoO}_2$. Then, we replaced Co with equal molar Co–Ti–Mn–Ni–Ru randomly. The chosen supercell contains ten formula units and 36 atoms. All distinct structures from the simulated annealing trace with 3000 Monte Carlo steps were then calculated using DFT. Those represent the lowest energy structures for the entire configuration space.

Na Diffusion Kinetics and Na Migration Barriers. The PBE³¹ generalized gradient approximation functional was adopted in density functional theory calculations using the Vienna Ab initio Simulation Package (VASP).^{32,33} Na migration barriers were calculated using the climbing-image nudged elastic-band (CINEB).³⁴ In this study, supercells of $4 \times 4 \times 1$ (32 formula units) were used for mixed and single TM systems. The k-point grid was generated following the automated k-mesh generation method. Each interpolated image was relaxed until the forces on each atom were less than 0.02 eV \AA^{-1} . To investigate the role of the transition metal on Na diffusion, we

performed CINEB calculations at the dilute Na concentration. In the P2 layered oxides, there are two kinds of Na sites. The Na(f) site shares faces with two TM oxide octahedra, and the Na(e) site shares only an edge with TM oxide octahedron. A total of 25 different Na(f) site configurations were created in the lattice of CoO_2 with Ni, Mn, Ru, and Ti as dopants, and considering TM species combinations. We calculated the Na(e)–Na(f)–Na(e) migration barriers for various Na(f) compositions. AIMD simulations were then carried out in the constant volume (NVT) ensemble at 1000 K with a Nosé–Hoover thermostat for 60 ps to elucidate the Na site occupancies and diffusion mechanism.³⁵ We conducted nonspin-polarized simulations with a smaller plane-wave energy cutoff of 300 eV and Γ -centered $1 \times 1 \times 1$ k-point grid to reduce computational costs. Two simulated annealing optimized structures were adopted in the AIMD simulations: one for the ground-state structure and the second for a low-energy structure with energy close to that of the ground-state.

3. RESULTS

3.1. Materials Synthesis and *in situ* XRD for Synthesis

The MPC layered oxide P2-TMCNR was successfully synthesized by a solid-state reaction guided by the information obtained from *in situ* XRD for synthesis. Figure 1 shows *in situ*

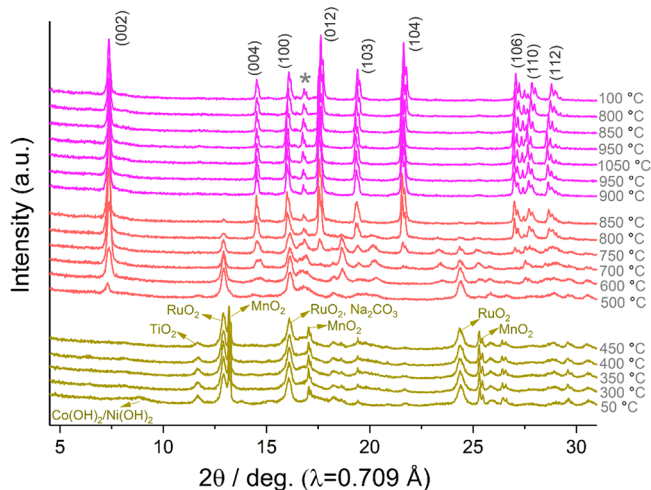


Figure 1. *In situ* XRD patterns of ball-milled precursor during the slow heating and quick cooling process in air. The indices of the reflections corresponding to the P2 phase are labeled in. The impurity rock-salt phase is labeled with an asterisk.

XRD patterns that were collected while the starting materials were slowly heated from 50 to 1050 °C and then quickly cooled to 100 °C. It is observed that $\text{Co}(\text{OH})_2$ and $\text{Ni}(\text{OH})_2$ precursors became amorphous after the ball-milling process, with only one broad characteristic peak at around 9° seen, while other precursors remain crystalline. No significant phase change was observed from 50 to 450 °C. Starting from 500 °C, the characteristic diffraction peak of the layered structure around 7.5° is seen, indicating the initial formation of the layered phase. When the temperature is further increased to 900 °C, the precursor materials are entirely consumed, and most reflections can be attributed to a dominant P2 phase with a minor impurity of rock-salt phase, which is labeled with the asterisk. While the as-formed P2 phase shows good stability when the temperature further increases to 1050 °C, the synthesis of pure P2 phase with high entropy components is tricky, as layered oxide has a very complicated phase diagram, and there are many equilibria between the target phase and undesired impurity phase. More *in situ* XRD experiments were

conducted in an attempt to eliminate the rock salt impurity. However, it seems that it is part of the thermodynamic equilibrium within this temperature range and a broader range of elemental compositions and thus cannot be completely eliminated.

3.2. Crystal Structural Analysis

High-resolution synchrotron X-ray diffraction (SXRD) measurement was performed to reveal more details in the structure. Figure 2a shows the Rietveld refinement against the synchrotron XRD data. The pattern was refined using the $P6_3/mmc$ space group with a perfect P2-type stacking. The minor impurity phase was tentatively assigned as $(\text{Mn}_{1/3}\text{Co}_{1/3}\text{Ni}_{1/3})\text{O}$. It is difficult to determine the type and ratio of transition metals in the rock salt phase as their ionic radii and X-ray scattering ability are very similar. The impurity is estimated to account for only 5.85 wt % of the sample. Random mixing of the five metals in the TM layer is also adopted in the refinement, supported by the fact that no apparent characteristic superstructure peaks resulted from ordering in the AB-plane are seen in the range of 5–7°. A model of the crystal structure based on the refinement is illustrated in Figure 2b, and the crystallographic information extracted from the Rietveld refinement is summarized in Table 1. The SEM images in Figure 2c and the inset of Figure 2a show that the particles of P2-TMCNR have plate-like shapes, which is typical for layered materials, with a size of about 1–4 μm . The element distribution was analyzed using energy dispersive spectroscopy (EDS) elemental mapping, as displayed in Figure 2d. The homogeneous distribution of the five elements confirms that there is no elemental enrichment/segregation in the primary phase.

3.3. Electrochemical Performance

The electrochemical performance of P2-TMCNR was evaluated in half cells using different cutoff voltages and various current rates. Selected galvanostatic charge–discharge curves in the first 30 cycles in the range of 1.5–4.5 V are shown in Figure 4a. A low charge capacity in the first charge is seen, which is expected for all Na-poor P2 cathodes. The reasonably high initial discharge capacity of 174 mAh g^{-1} at 10 mA g^{-1} current density is achieved, which is corresponding to 0.72 Na extraction per mol P2-TMCNR. The voltage curve is sloping below 4.0 V, and one small voltage plateau above 4.0 V is observed in the first and second cycles. This plateau, however, is not seen in the following cycles, possibly due to a nonreversible structural change associated with oxygen evolution (O_2 release or lattice O redox), which is typically seen in the layered oxides at high voltage. These observations are in line with the two pronounced anodic peaks in the first cyclic voltammogram (CV) curve (Figure 4b), which merge in one broad peak at around ~ 4.1 V in the second cycle and gradually become broader in the following cycles. Correspondingly, two asymmetric cathodic peaks are found in the first two cycles, which shift to lower voltage and merge into one broad peak at ~ 2.9 V. Such irreversible evolution of the redox peaks in the CV profiles indicates that some sort of relaxation/rearrangement of the crystal structure is taking place in the first few cycles, which may be associated with the different trend of migration of the five cations under the driving forces in high voltage or due to the surface effects induced by the different migration rate of the cations.^{36,37}

The most exciting electrochemical performance of P2-TMCNR is its rate capability. Figure 4c shows the charge/

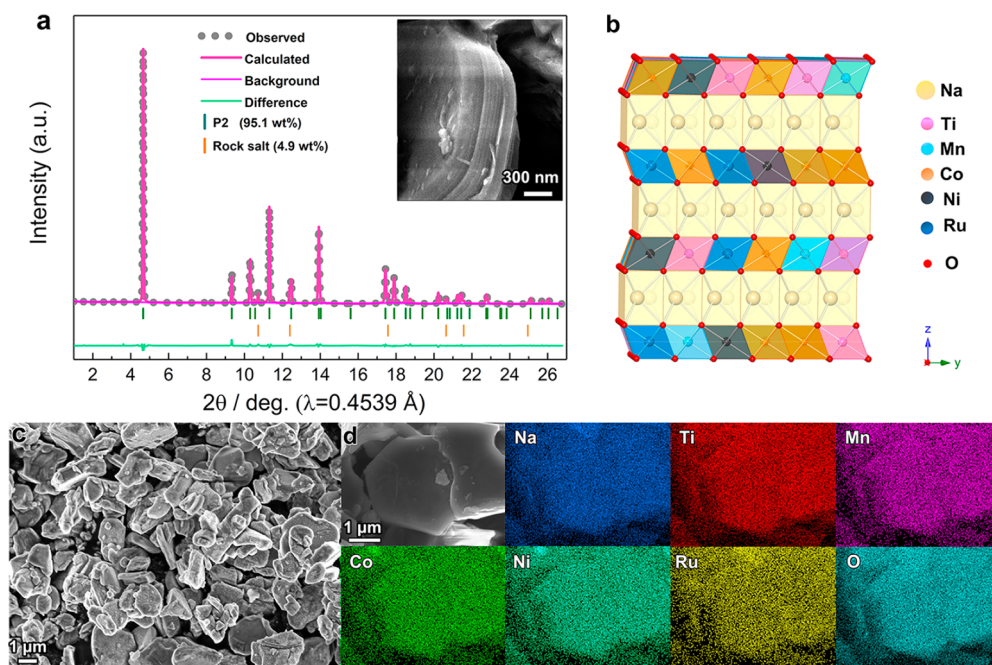


Figure 2. XRD and SEM of P2-TMCNR material. (a) SXRCD and Rietveld refinement of the P2-TMCNR sample, inset in (a) shows the high magnification side view of particles. (b) The crystal structure of P2-TMCNR was drawn based on the refined model. (c) Low magnification SEM image of the P2-TMCNR sample. (d) EDS mapping of the P2-TMCNR sample and the corresponding SEM image.

Table 1. Crystallographic Information of As-Prepared P2-TMCNR Sample Extracted from Rietveld Refinement

atom	Wyckoff	x	y	z	occ.	U_{iso}
Na _e	2d	0.3333	0.6667	0.75	0.401(8)	0.0281(2)
Na _f	2b	0	0	0.25	0.198(2)	0.0228 (3)
Ti	2a	0	0	0	0.2	0.0092(8)
Mn	2a	0	0	0	0.2	0.0126(7)
Co	2a	0	0	0	0.2	0.0110(6)
Ni	2a	0	0	0	0.2	0.0117(6)
Ru	2a	0	0	0	0.2	0.0172(4)
O	4f	0.3333	0.6667	0.0936(0)	0.953(3)	0.0152(2)

$a = b = 2.91455(1) \text{ \AA}$, $c = 11.13772(9) \text{ \AA}$, $V = 81.936(1) \text{ \AA}^3$, $\alpha = \beta = 90$, $\gamma = 120$

atom	Wyckoff	x	y	z	occ.	U_{iso}
Mn	4a	0	0	0	0.3333	0.0010(2)
Co	4a	0	0	0	0.3333	0.0038(1)
Ni	4a	0	0	0	0.3333	0.0234(1)
O	4b	0.5	0.5	0.5	1	0.0057(2)

5.85 wt % rock-salt phase ($Fm\bar{3}m$)
 $a = b = c = 4.19875(8) \text{ \AA}$, $\alpha = \beta = \gamma = 90$, $V = 74.022(4) \text{ \AA}^3$
 $R_{wp} = 2.77\%$, $R_p = 1.86\%$, $\chi^2 = 1.531$

discharge profiles of P2-TMCNR cycled at various current densities. By comparing with the electrochemical curves of the Ni and Mn containing layered oxides reported previously, such as $\text{NaNi}_{0.5}\text{Mn}_{0.5}\text{O}_2$,³⁸ $\text{Na}_x\text{Ni}_{1/3}\text{Co}_{1/3}\text{Mn}_{1/3}\text{O}_2$,³⁹ $\text{Na}_{0.67}\text{Cu}_{0.15}\text{Ni}_{0.2}\text{Mn}_{0.65}\text{O}_2$,⁴⁰ $\text{NaNi}_{0.45}\text{Cu}_{0.05}\text{Mn}_{0.4}\text{Ti}_{0.1}\text{O}_2$,³⁸ $\text{Na}_{1.2}\text{Ni}_{0.2}\text{Mn}_{0.2}\text{Ru}_{0.4}\text{O}_2$,⁴¹ $\text{Na}(\text{Ni}_{0.25}\text{Co}_{0.25}\text{Fe}_{0.25}\text{Ti}_{0.25})\text{O}_2$,⁴² and $\text{Na}(\text{Mn}_{0.25}\text{Fe}_{0.25}\text{Co}_{0.25}\text{Ni}_{0.25})\text{O}_2$,⁴³ in which multiple plateaus in steps are noticeably involved, whereas the P2-TMCNR shows smooth and sloping discharge profiles. The smooth and plateau-less voltage profiles feature are due to the lack of sodium ion/vacancy ordering in the electrode materials upon cycling, corresponding to a predominant solid solution-type phase evolution pathway, which can be beneficial for sodium ion mobility in the layered structures.

P2-TMCNR demonstrates a superior rate performance, which exhibits a discharge capacity of 164, 150, 142, 128, 100, and 89 mAh g^{-1} at current densities of 20, 200, 1000, 2000, 5000, and 8000 mA g^{-1} , respectively. These current densities correspond to 0.1, 1.2, 5.8, 11.5, 29, and 46 C by applying the first discharge capacity of 174 mAh g^{-1} at a low rate as the standard of 1 C rate, respectively. When extending the lower cutoff voltage to 1 V to compensate for the ohmic voltage drop, P2-TMCNR can deliver fairly high capacities of 78 and 68 mAh g^{-1} at 10 000 mA g^{-1} (57 C) and 15 000 mA g^{-1} (86 C) respectively (Figure 3c). These outstanding rate performances put P2-TMCNR among the best high rate cathode materials for NIBs (Table S1).

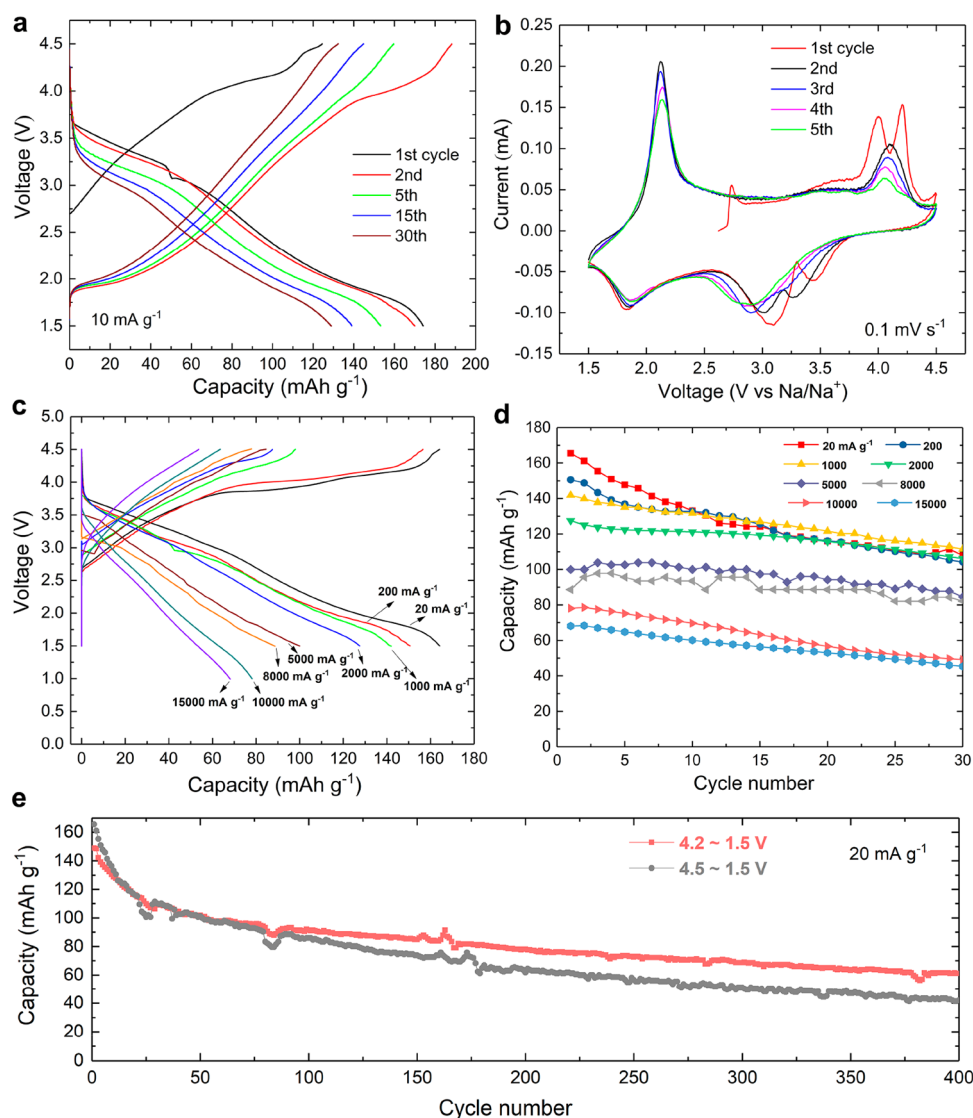


Figure 3. Electrochemical performances of P2-TMCNR in half cells: (a) selected galvanostatic charge and discharge curves in the first 30 cycles at current density of 10 mA g^{-1} , (b) the initial five cycles of cyclic voltammograms of the P2-TMCNR cathode, (c) charge and discharge curves at different rates, (d) cycling performances at various rates, and (e) long-term cycling performance in different voltage ranges at 20 mA g^{-1} .

The capacity retention of P2-TMCNR, however, is not ideal. Long-term cycling tests were conducted under various rates and voltage windows. Figure 3d shows cycling performances at different rates. Noticeable capacity degradation during the initial 30 cycles is observed in all tests, indicating unsatisfied cycling stability for this compound, likely due to the undesired irreversible structural changes at high voltage range as found in previously reported P2-type layered compounds during the sodiation/desodiation process.^{17,44,45} We further compare the cycle life of P2-TMCNR cycled at 20 mA g^{-1} in two different voltage windows, 1.5–4.5 V and 1.5–4.2 V (Figure 3e). The cell shows better capacity retention with a lower upper cutoff voltage of 4.2 V than a higher upper cutoff of 4.5 V, which implies that high voltage is plausibly destructive to the pristine crystal structure. It is also worth noting that most capacity fading takes place in the first 20–40 cycles. The capacity retention in the following cycle is not as significant. In the 1.5–4.2 V cycling, with an initial capacity of 149 mAh g^{-1} and a capacity of 61 mAh g^{-1} after 400 cycles, the capacity retention rate per cycle is 99.78%. The capacity retention rate from the

40th cycle (104 mAh/g) to the 400th cycle (61 mAh/g) is much higher at 99.85%.

3.4. Operando XRD Analysis

To understand the detailed structural evolution of P2-TMCNR upon sodium extraction/insertion, *operando* XRD measurement was conducted at a C/30 rate with a lab X-ray source. The *in situ* cell exhibits charge/discharge capacities of $153/195 \text{ mAh g}^{-1}$ and $227/190 \text{ mAh g}^{-1}$ in the first and second cycles, respectively, which are slightly better than the data collected from coin cells as the *in situ* cell has higher pressure and runs at a slower rate. Figure 4 shows *in situ* XRD patterns and the corresponding voltage curves for the first two cycles. In the low voltage regions (below 4.1 V), a solid solution like evolution is observed in both charging and discharging, as evidenced by the shifting of all Bragg peaks, particularly the shifting of the (002) peaking, which indicating the *d*-spacing along *c*-direction between the TM and Na slabs. The (002) peak shifts to lower *d*-spacing as more Na is extracted from the lattice, indicating a greater *d*-spacing along *c*-direction resulting from less attraction among Na^+ and O^{2-} . Meanwhile, the AB-plane is shrinking due to less

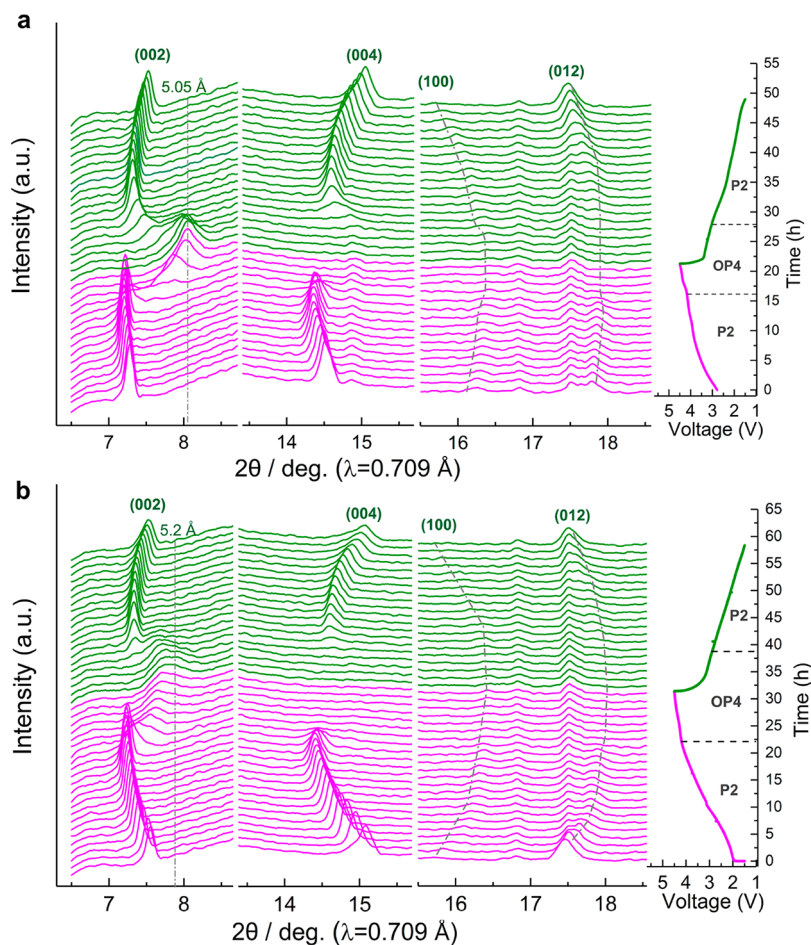


Figure 4. Operando XRD patterns collected during the first (a) and second (b) charge/discharge process of P2- Na_xTMCNR at a current rate of $C/30$ (left) along with an illustration of sodium contents versus voltage of the cell upon cycling on the right.

repulsion among Na^+ in the same plane, evidenced by the moving toward higher 2θ of the (100) and (102) peaks. However, at a higher state of charge (low Na concentration), the (002) reflection moves slightly to a higher angle (smaller d -spacing) and disappears at 4.14 V ($x_{\text{Na}} = 0.146$), accompanied by the vanishing of (004) and (012) reflections and the emerging of a new broad peak with smaller d -spacing and continuously shifting to higher 2θ until the end of charge at 4.5 V. This broad peak does not belong to the commonly seen O2 phase in the cycling of P2 cathode, as the d -spacing of the O2 phase is much smaller (around 4.44 Å).⁴⁶ We suspect that this new phase is the “OP4” phase, which is also seen in the cycling of other P2 cathodes at low Na content. The OP4 phase can be described as a continuously changing intergrowth of P2 and O2 slabs with OP4 as an intermediate phase.⁴⁶ At high voltage with low Na concentration, gliding of slabs from P2-type stacking (ABBA oxygen stacking) to O2-type stacking (ABAC) with a smaller d -spacing can take place in two crystallographic equivalents but spatially different ways with a gliding vector of either $(1/3, 2/3, 0)$ or $(2/3, 1/3, 0)$.⁴⁷ Such gliding is not coordinated throughout each single particle as Na extraction can be simultaneous yet inhomogeneous at any active surface of the particle. Therefore, the long-range ordering is lost, and a nanodomain-like feature forms inside the particles, which results in much lower and broader Bragg peaks than long-range well-ordered pristine particles.

As shown in Figure 4a, the P2 phase remains up to a Na concentration of $x = 0.146$ at 4.14 V, where the OP4 phase starts to form, which is corresponding to the voltage plateau above 4.1 V in the voltage profiles. After charging up to 4.5 V, the OP4 phase slowly and reversibly turns into a single P2 phase in discharge until 1.5 V. In the second cycle, the evolution of the Bragg peaks presents a trend similar to that of the first cycle, whereas the OP4 phase exhibits a larger d -spacing at 4.5 V, as shown in Figure 4b. This might imply that some migration of transition metals driven by the high voltage takes place in the first cycle so that the d -spacing change is less significant at high voltage in the second cycle, which may also be responsible for the capacity fading and the large polarization. It is also worth noting that, upon the first two cycles, no signature reflection peaks corresponding to either the Na or TM ordering are observed, nor the P'2 phase with monoclinic distortion within the whole range of Na (de)intercalation. This observation is further confirmed by *ex situ* SXRD of the electrode materials collected at various state of charge (Figure S1). Despite the possible TM migration and the P2–OP4 phase transition, the dominant P2 phase in the materials is retained after 100 cycles of charge–discharge at 20 mA g^{-1} (Figure S2 and Table S2), demonstrating a reasonably good long-range structural stability.

3.5. Monte Carlo Simulations

The thermodynamics and diffusion kinetics of the MPC P2-TMCNR cathode were further investigated using Monte Carlo

simulations with previously trained graph-based deep learning MEGNet models. First, various structures were sampled using Monte Carlo simulations, and the MEGNet model predictions were validated using DFT calculations, indicating good agreement between the MEGNet results and those of the DFT predictions (see Tables S3 and S4 and Figures S3 and S4 for details). In particular, the predicted face-sharing Na(f) site energy is higher than the edge-sharing Na(e) site energy by 110 meV/atom, close to the DFT value of 130 meV/atom. This result agrees qualitatively with the Rietveld refinement results against the synchrotron XRD for the structure with Na overall fraction of 0.60, where the occupancies of Na(e) and Na(f) are ~ 0.40 and ~ 0.20 , respectively. Overall, the MEGNet formation energy model is sufficiently accurate to be used for a preliminary identification of potential low energy structures using simulated annealing, which is then further evaluated using accurate DFT calculations, as shown in the distribution in Figure 5.

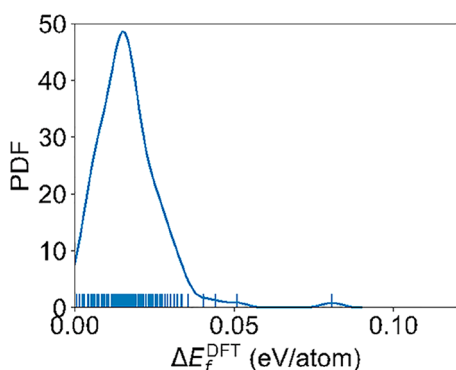


Figure 5. Probability distribution function (PDF) of DFT-calculated formation energy above the ground state (GS), i.e., $\Delta E_f = E_f - E_f^{\text{GS}}$ for low-energy orderings of TMs and Na found by simulated annealing.

The distribution in Figure 5 has a full width at half maximum within 30 meV/atom, close to the thermal energy at room temperature ~ 26 meV/atom. This small energy spread suggests that all those states can be reached via thermal excitation even at room temperature. In addition, the entropic

contribution to the overall free energy is -41.4 meV/atom for TM disordering and is -71.6 meV/atom if including Na disordering (eq S1) in P2-TMCNR. Such large free energy driven force will negate the small enthalpy spread, favoring the formation of TM and Na disordered compounds. Sarker et al.⁴⁸ earlier proposed an entropy forming ability (EFA) in metal carbides (MoNbTaVWC₅ and other carbides with fewer metal cations), defined as the reciprocal of degeneracy-corrected standard deviation for computed energy distribution spectrum. The authors found that with an EFA value above 67 (eV/atom)⁻¹, single-phase compounds could be synthesized experimentally, and multiphase is detected when EFA is below 45 (eV/atom)⁻¹. The computed EFA from the distribution in Figure 5 is approximately 98.4 (eV/atom)⁻¹ without considering the degeneracy, suggesting that high entropy compounds with both Na and TM disordering can be formed.

Given that Na(f) sites are higher in energy than Na(e) sites in general, CINEB calculations were performed for Na(e)–Na(f)–Na(e) migration paths, where the Na(f) site is the transition state. Here, we will refer to a Na(f) site that shares faces with a MO₆ and M'O₆ as a Na(f)_{M–M'} site for brevity. Figure 6a summarizes the Na migration barriers of different Na(f)_{M–M'}. It may be observed that Na(f) sites that share faces with NiO₆ and/or CoO₆ have the lowest migration barriers. For example, Na(f)_{Ni–Ni} sites have the lowest migration barriers of 89 meV, while Na(f)_{Ni–Co} and Na(f)_{Co–Co} sites have slightly higher migration barriers of 103–105 meV. Ti and Mn containing Na(f) sites have intermediate diffusion barriers. However, the presence of Ru results in much higher migration barriers. These observations are consistent with the AIMD trajectories, which show that Ti–Ru sites are the least preferred (Figure 6b). In previous work, some of the present coauthors have established that the diffusion topology in the P2 lattice can be modeled based on an effective triangular lattice of Na(f) sites, which has an analytical site percolation threshold p_c of 0.5. For fast macroscopic diffusion in the P2 framework, TMs that result in high Na migration barriers should therefore be kept to a concentration < 0.293 , while TMs that result in low Na migration barriers should have a concentration > 0.293 .²² In P2-TMCNR, the concentration of detrimental Ru is < 0.293 , while the combined concentration of

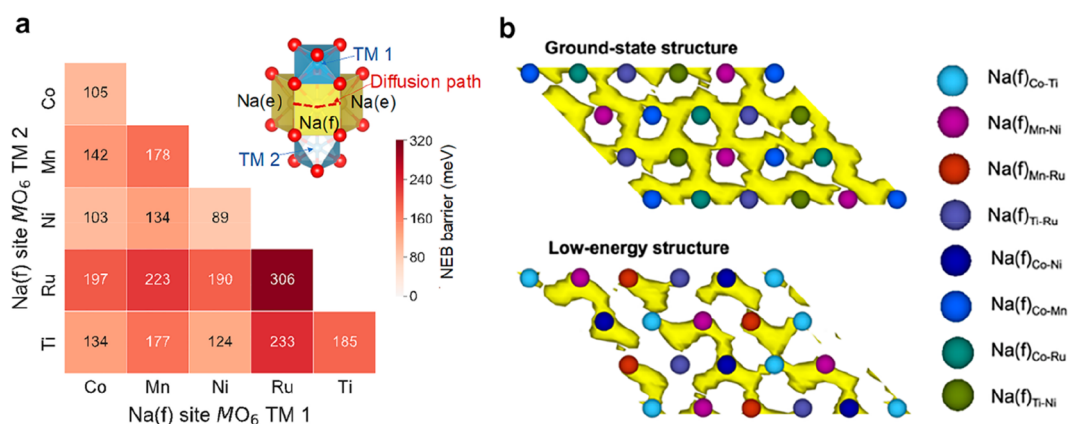


Figure 6. (a) Na(e)–Na(f)–Na(e) single Na hopping migration barriers (meV) of different Na(f) site compositions at the fully charged limit. (b) Isosurfaces of Na ion (yellow) probability density distribution P at $P = P_{\text{max}}/32$ for P2-TMCNR at 1000 K of AIMD trajectories for the ground-state structure and a low-energy structure of P2-TMCNR with Na(f)_{Ti–Ru} sites. The configurations are visualized from the top view on the AB-plane. The color scheme of circles corresponds to different Na(f) site configurations. The Na probability density distribution was obtained by averaging the Na occupation on a uniform grid over the trajectories during the AIMD simulation of 20 ps following the thermal equilibration period.

beneficial Co and Ni is >0.293 , i.e., the percolation thresholds for fast macroscopic diffusion are satisfied.

4. DISCUSSION

Motivated by reducing the possible ordering and phase transition in the cycling of the P2-structure cathode, we designed this P2-TMNCr cathode as an early exploration toward the promising group of MPC or high entropy compounds. The choice of the five transition metals is based on design principles considering charge compensation, favorable Na content, theoretical capacity, etc. and further screened by experimental trials. Certainly, this is not the only multiprincipal component composition that works, nor that works best. It is plausible that other compositions can stabilize the P2 structure and will be identified in the future. However, the present composition offers an opportunity for an initial exploration into this class of materials.

It delivers reasonably high initial capacity, average capacity retention, and surprisingly high rate performance, indicating the strong promise along this direction. With a joint experimental and theoretical investigation, we revealed the underlying mechanism of this high rate capability. First, the high entropy TM mixing in the layered P2 oxides creates a TM cation disorder and $TM^{n+}/TM^{(n+1)+}$ charge disorder within the TM slabs, which exert disruption on the Na-site energy. It impedes the formation of Na-ion/vacancy ordering in the lattice and promotes a dominant solid solution behavior for the Na (de)intercalation, which is very beneficial for both structural stability and Na diffusion. This P2 compound presents a smooth and sloping charge/discharge curve under 4.1 V, while many P2 compounds show multiple voltage steps and plateaus. The TM disordering and Na disordering are validated by both the MEGNet computation and XRD analysis. Second, the low concentration of Mn in the high entropy P2 compound restrains the monoclinic transition in the Mn containing materials at the end of discharge (1.5 V). It prevents the occurrence of phase transition from P2 to P'2 phase that is resulted from the strong collective Jahn–Teller effect of Mn^{3+} .⁴⁴ Although the occurrence of the phase transition between P2 and OP4 is observed in the P2-TMNCr at the high voltage region (>4.1 V), it has been well demonstrated by multiple previous studies that the rate-limiting process of P2 cathodes is the end-of-discharge process, rather than the end-of-charge structural transformation.^{17,49,50}

More importantly, detailed computational evaluation shows that the fraction of low-diffusion barrier domains in P2-TMNCr is within the theoretical bounds of the site-percolation model,²² which allows fast macroscopic diffusion of Na ions within a single crystalline particle. For a layered oxide cathode with fewer TM cations in the TM layer, high diffusion barrier domains can rather easily block the percolation of the fast diffusion pathways due to the high possibility of occurrence of ordering among the fewer types of cations. While in the high entropy cathode, first, it is more difficult to form predominant ordering throughout the single crystalline particles. Second, the much more abundant number of configurations mitigates the blocking effect of the high diffusion barrier domains. By rationally designing and selecting the TM cations, it is possible to form a percolating fast diffusion pathway at macroscopic level, such as demonstrated by P2-TMNCr.

Of course, the composition and elemental ratio in P2-TMNCr is not necessarily optimal, and further rational design

around the high entropy approach is desired and promising at the same time. The high entropy composition brings more complexity to the investigation but also more room in design. With the computational evaluation results, better combinations of TMs can be expected, offering the possibility of even higher diffusivity. On the other hand, the experimental results also indicate that capacity degradation is non-negligible, plausibly associated with the transition metal migration⁵¹ and dissolution,⁵² oxygen evolution and lattice rearrangement at high voltage range,^{17,45} as well as the undesired electrode–electrolyte parasitic reactions.^{53,54} The exact degradation mechanism is still not clearly understood at this point. Based on the *ex situ* XRD on P2-TMNCr after 100 cycles of charge/discharge, as shown in Figure S2, no obvious long-range ordering change is observed, implying the detrimental structural changes might be subtle, local, or at/near the surface, which calls for more microscopic and local structure investigations in the future.

5. CONCLUSION

In summary, we designed and prepared a high entropy layered sodium TM oxide, P2-TMNCr, which was studied as a cathode material in a Na-ion battery for the first time, in an attempt to suppress Na^+ /vacancy ordering occurring during sodiation–desodiation processes. It exhibits a good capacity of 68 mAh g^{-1} at a surprisingly high current density of 86 C (15 000 mA g^{-1}), exceeding most previously reported layered oxide cathode materials. The excellent rate performance of P2-TMNCr benefits from the high entropy composition because (1) the ordering of Na^+ /vacancy is mitigated due to a disordered distribution of cations in the TM layer and (2) a percolating low-barrier diffusion network is created, revealed by the computational evaluations. Although, as one of the early trials in high entropy designs in cathodes of NIBs, P2-TMNCr is not satisfactory in all performance categories, the outstanding rate performance and the promise of further improvement in long-term cycling stability warrants further study along this direction and opens up a great deal of opportunities.

■ ASSOCIATED CONTENT


SI Supporting Information


The Supporting Information is available free of charge at <https://pubs.acs.org/doi/10.1021/jacsau.0c00002>.

Rate performance comparison between various high rate cathodes for SIBs, SXRD patterns of the P2-TMNCr cathode at different states of charge for the first cycle, detailed XRD refinement results of cathode cycled 100 cycles, and MEGNet results validation (PDF)

■ AUTHOR INFORMATION

Corresponding Authors

Hailong Chen – *The Woodruff School of Mechanical Engineering, Georgia Institute of Technology, Atlanta, Georgia 30332-0245, United States*;  orcid.org/0000-0001-8283-2860; Email: hailong.chen@me.gatech.edu

Shyue Ping Ong – *Nanoengineering Department, University of California, San Diego, La Jolla, California 92093, United States*;  orcid.org/0000-0001-5726-2587; Email: ongsp@eng.ucsd.edu

Authors

Lufeng Yang – *The Woodruff School of Mechanical Engineering, Georgia Institute of Technology, Atlanta, Georgia 30332-0245, United States*

Chi Chen – *Nanoengineering Department, University of California, San Diego, La Jolla, California 92093, United States*

Shan Xiong – *The Woodruff School of Mechanical Engineering, Georgia Institute of Technology, Atlanta, Georgia 30332-0245, United States*

Chen Zheng – *Nanoengineering Department, University of California, San Diego, La Jolla, California 92093, United States*

Pan Liu – *School of Earth and Atmospheric Sciences, Georgia Institute of Technology, Atlanta, Georgia 30332-0340, United States*

Yifan Ma – *The Woodruff School of Mechanical Engineering, Georgia Institute of Technology, Atlanta, Georgia 30332-0245, United States*

Wenqian Xu – *X-ray Science Division, Advanced Photon Source, Argonne National Laboratory, Lemont, Illinois 60439, United States*

Yuanzhi Tang – *School of Earth and Atmospheric Sciences, Georgia Institute of Technology, Atlanta, Georgia 30332-0340, United States; orcid.org/0000-0002-7741-8646*

Complete contact information is available at:
<https://pubs.acs.org/10.1021/jacsau.0c00002>

Author Contributions

[#]L.Y. and C.C. contributed equally to this work.

Notes

The authors declare no competing financial interest.

ACKNOWLEDGMENTS

L.Y., S.X., Y.M., and H.C. acknowledge financial support from the NSF under Grant 1706723 and the Georgia Tech new faculty startup fund. This research used Beamline 17-BM of the Advanced Photon Source, a U.S. DOE Office of Science User Facility operated for the DOE Office of Science by Argonne National Laboratory under Contract DE-AC02-06CH11357. C.C., C.Z., and S.P.O. acknowledge the support from the Materials Project, funded by the U.S. Department of Energy, Office of Science, Office of Basic Energy Sciences, Materials Sciences and Engineering Division under Contract DE-AC02-05-CH11231: Materials Project program KC23MP. The authors acknowledge Dr. Jianming Bai for help in synchrotron data collection at the XPD (28-ID-2) beamline of the National Synchrotron Light Source II, a U.S. Department of Energy (DOE) Office of Science User Facility operated for the DOE Office of Science by Brookhaven National Laboratory under Contract DE-SC0012704. The authors also acknowledge Dr. Bart A. Johnson and Dr. Donata Passarello for help in synchrotron data collection at the Stanford Synchrotron Radiation Lightsource, SLAC National Accelerator Laboratory, which is supported by the U.S. Department of Energy, Office of Science, Office of Basic Energy Sciences under Contract DE-AC02-76SF00515.

REFERENCES

(1) Kubota, K.; Kumakura, S.; Yoda, Y.; Kuroki, K.; Komaba, S. *Adv. Energy Mater.* **2018**, *8*, 1703415.

- (2) Delmas, C.; Fouassier, C.; Hagenmuller, P. *Physica B+C* **1980**, *99*, 81.
- (3) Bai, Q.; Yang, L.; Chen, H.; Mo, Y. *Adv. Energy Mater.* **2018**, *8*, 1702998.
- (4) Ong, S. P.; Chevrier, V. L.; Hautier, G.; Jain, A.; Moore, C.; Kim, S.; Ma, X.; Ceder, G. *Energy Environ. Sci.* **2011**, *4*, 3680.
- (5) Wang, Y.; Xiao, R.; Hu, Y.-S.; Avdeev, M.; Chen, L. *Nat. Commun.* **2015**, *6*, 1.
- (6) Clément, R. J.; Bruce, P. G.; Grey, C. P. *J. Electrochem. Soc.* **2015**, *162*, A2589.
- (7) Berthelot, R.; Carlier, D.; Delmas, C. *Nat. Mater.* **2011**, *10*, 74.
- (8) Vinckeviciute, J.; Radin, M. D.; Van der Ven, A. *Chem. Mater.* **2016**, *28*, 8640.
- (9) Chou, F.; Chu, M.-W.; Shu, G.; Huang, F.-T.; Pai, W. W.; Sheu, H.; Lee, P. A. *Phys. Rev. Lett.* **2008**, *101*, 127404.
- (10) Medarde, M.; Mena, M.; Gavilano, J.; Pomjakushina, E.; Sugiyama, J.; Kamazawa, K.; Pomjakushin, V. Y.; Sheptyakov, D.; Batlogg, B.; Ott, H. *Phys. Rev. Lett.* **2013**, *110*, 266401.
- (11) Wang, P.-F.; Yao, H.-R.; Liu, X.-Y.; Yin, Y.-X.; Zhang, J.-N.; Wen, Y.; Yu, X.; Gu, L.; Guo, Y.-G. *Science advances* **2018**, *4*, No. eaar6018.
- (12) Li, Y.; El Gabaly, F.; Ferguson, T. R.; Smith, R. B.; Bartelt, N. C.; Sugar, J. D.; Fenton, K. R.; Cogswell, D. A.; Kilcoyne, A. D.; Tylliszczak, T. *Nat. Mater.* **2014**, *13*, 1149.
- (13) Yang, L.; Li, X.; Liu, J.; Xiong, S.; Ma, X.; Liu, P.; Bai, J.; Xu, W.; Tang, Y.; Hu, Y.-Y. *J. Am. Chem. Soc.* **2019**, *141*, 6680.
- (14) Radin, M. D.; Alvarado, J.; Meng, Y. S.; Van der Ven, A. *Nano Lett.* **2017**, *17*, 7789.
- (15) Li, X.; Ma, X.; Su, D.; Liu, L.; Chisnell, R.; Ong, S. P.; Chen, H.; Toumar, A.; Idrobo, J.-C.; Lei, Y. *Nat. Mater.* **2014**, *13*, 586.
- (16) Yang, L.; Li, X.; Ma, X.; Xiong, S.; Liu, P.; Tang, Y.; Cheng, S.; Hu, Y.-Y.; Liu, M.; Chen, H. *J. Power Sources* **2018**, *381*, 171.
- (17) Liu, L.; Li, X.; Bo, S. H.; Wang, Y.; Chen, H.; Twu, N.; Wu, D.; Ceder, G. *Adv. Energy Mater.* **2015**, *5*, 1500944.
- (18) Mu, L. Q.; Feng, X.; Kou, R. H.; Zhang, Y.; Guo, H.; Tian, C. X.; Sun, C. J.; Du, X. W.; Nordlund, D.; Xin, H. L. L.; Lin, F. *Adv. Energy Mater.* **2018**, *8*, 1801975.
- (19) Mu, L. Q.; Hou, Q. P.; Yang, Z. Z.; Zhang, Y.; Rahman, M. M.; Kautz, D. J.; Sun, E.; Du, X. W.; Du, Y. G.; Nordlund, D.; Lin, F. *J. Electrochem. Soc.* **2019**, *166*, A251.
- (20) Rahman, M. M.; Mao, J.; Kan, W. H.; Sun, C.-J.; Li, L.; Zhang, Y.; Avdeev, M.; Du, X.-W.; Lin, F. *Acs Materials Letters* **2019**, *1*, 573.
- (21) Rahman, M. M.; Xu, Y. H.; Cheng, H.; Shi, Q. L.; Kou, R. H.; Mu, L. Q.; Liu, Q.; Xia, S. H.; Xiao, X. H.; Sun, C. J.; Sokaras, D.; Nordlund, D.; Zheng, J. C.; Liu, Y. J.; Lin, F. *Energy Environ. Sci.* **2018**, *11*, 2496.
- (22) Zheng, C.; Radhakrishnan, B.; Chu, I.-H.; Wang, Z.; Ong, S. P. *Phys. Rev. Appl.* **2017**, *7*, 064003.
- (23) Lei, Y.; Li, X.; Liu, L.; Ceder, G. *Chem. Mater.* **2014**, *26*, 5288.
- (24) Gludovatz, B.; Hohenwarter, A.; Catoor, D.; Chang, E. H.; George, E. P.; Ritchie, R. O. *Science* **2014**, *345*, 1153.
- (25) Jiang, S.; Hu, T.; Gild, J.; Zhou, N.; Nie, J.; Qin, M.; Harrington, T.; Vecchio, K.; Luo, J. *Scr. Mater.* **2018**, *142*, 116.
- (26) Wang, Q.; Sarkar, A.; Li, Z.; Lu, Y.; Velasco, L.; Bhattacharya, S. S.; Brezesinski, T.; Hahn, H.; Breitung, B. *Electrochem. Commun.* **2019**, *100*, 121.
- (27) Zhao, C.; Ding, F.; Lu, Y.; Chen, L.; Hu, Y. S. *Angew. Chem., Int. Ed.* **2020**, *59*, 264.
- (28) Ma, X.; An, K.; Bai, J.; Chen, H. *Sci. Rep.* **2017**, *7*, 1.
- (29) Chen, C.; Ye, W.; Zuo, Y.; Zheng, C.; Ong, S. P. *Chem. Mater.* **2019**, *31*, 3564.
- (30) Jain, A.; Ong, S. P.; Hautier, G.; Chen, W.; Richards, W. D.; Dacek, S.; Cholia, S.; Gunter, D.; Skinner, D.; Ceder, G. *APL Mater.* **2013**, *1*, 011002.
- (31) Perdew, J. P.; Burke, K.; Ernzerhof, M. *Phys. Rev. Lett.* **1996**, *77*, 3865.
- (32) Botana, A. S.; Norman, M. R. *Physical Review Materials* **2019**, *3*, 044001.
- (33) Kresse, G.; Furthmüller, J. *Comput. Mater. Sci.* **1996**, *6*, 15.

- (34) Henkelman, G.; Uberuaga, B. P.; Jónsson, H. *J. Chem. Phys.* **2000**, *113*, 9901.
- (35) Nosé, S. *J. Chem. Phys.* **1984**, *81*, 511.
- (36) Yan, P.; Zheng, J.; Zhang, J.-G.; Wang, C. *Nano Lett.* **2017**, *17*, 3946.
- (37) Yan, P.; Zheng, J.; Tang, Z.-K.; Devaraj, A.; Chen, G.; Amine, K.; Zhang, J.-G.; Liu, L.-M.; Wang, C. *Nat. Nanotechnol.* **2019**, *14*, 602.
- (38) Yao, H.-R.; Wang, P.-F.; Gong, Y.; Zhang, J.; Yu, X.; Gu, L.; OuYang, C.; Yin, Y.-X.; Hu, E.; Yang, X.-Q. *J. Am. Chem. Soc.* **2017**, *139*, 8440.
- (39) Xu, G.-L.; Amine, R.; Xu, Y.-F.; Liu, J.; Gim, J.; Ma, T.; Ren, Y.; Sun, C.-J.; Liu, Y.; Zhang, X. *Energy Environ. Sci.* **2017**, *10*, 1677.
- (40) Kang, W.; Yu, D. Y.; Lee, P.-K.; Zhang, Z.; Bian, H.; Li, W.; Ng, T.-W.; Zhang, W.; Lee, C.-S. *ACS Appl. Mater. Interfaces* **2016**, *8*, 31661.
- (41) Su, N.; Lyu, Y.; Guo, B. *Electrochem. Commun.* **2018**, *87*, 71.
- (42) Yue, J.-L.; Zhou, Y.-N.; Yu, X.; Bak, S.-M.; Yang, X.-Q.; Fu, Z.-W. *J. Mater. Chem. A* **2015**, *3*, 23261.
- (43) Li, X.; Wu, D.; Zhou, Y.-N.; Liu, L.; Yang, X.-Q.; Ceder, G. *Electrochem. Commun.* **2014**, *49*, 51.
- (44) Mortemard de Boisse, B.; Carlier, D.; Guignard, M.; Bourgeois, L.; Delmas, C. *Inorg. Chem.* **2014**, *53*, 11197.
- (45) Talaie, E.; Duffort, V.; Smith, H. L.; Fultz, B.; Nazar, L. F. *Energy Environ. Sci.* **2015**, *8*, 2512.
- (46) Somerville, J. W.; Sobkowiak, A.; Tapia-Ruiz, N.; Billaud, J.; Lozano, J. G.; House, R. A.; Gallington, L. C.; Ericsson, T.; Häggström, L.; Roberts, M. R. *Energy Environ. Sci.* **2019**, *12*, 2223.
- (47) Kubota, K.; Yoda, Y.; Komaba, S. *J. Electrochem. Soc.* **2017**, *164*, A2368.
- (48) Sarker, P.; Harrington, T.; Toher, C.; Oses, C.; Samiee, M.; Maria, J.-P.; Brenner, D. W.; Vecchio, K. S.; Curtarolo, S. *Nat. Commun.* **2018**, *9*, 1.
- (49) Clément, R. J.; Billaud, J.; Armstrong, A. R.; Singh, G.; Rojo, T.; Bruce, P. G.; Grey, C. P. *Energy Environ. Sci.* **2016**, *9*, 3240.
- (50) Sharma, N.; Tapia-Ruiz, N.; Singh, G.; Armstrong, A. R.; Pramudita, J. C.; Brand, H. E.; Billaud, J.; Bruce, P. G.; Rojo, T. *Chem. Mater.* **2015**, *27*, 6976.
- (51) Talaie, E.; Kim, S. Y.; Chen, N.; Nazar, L. F. *Chem. Mater.* **2017**, *29*, 6684.
- (52) Rahman, M. M.; Mao, J.; Kan, W. H.; Sun, C.-J.; Li, L.; Zhang, Y.; Avdeev, M.; Du, X.-W.; Lin, F. *ACS Materials Letters* **2019**, *1*, 573.
- (53) Song, J. H.; Xiao, B. W.; Lin, Y. H.; Xu, K.; Li, X. L. *Adv. Energy Mater.* **2018**, *8*, 1703082.
- (54) Song, J. H.; Wang, K.; Zheng, J. M.; Engelhard, M. H.; Xiao, B. W.; Hu, E. Y.; Zhu, Z. H.; Wang, C. M.; Sui, M. L.; Lin, Y. H.; Reed, D.; Sprenkle, V. L.; Yan, P. F.; Li, X. L. *Acs Energy Letters* **2020**, *5*, 1718.